ACS APPLIED MATERIALS & INTERFACES

Research Article

www.acsami.org

Coralloid $Co_2P_2O_7$ Nanocrystals Encapsulated by Thin Carbon Shells for Enhanced Electrochemical Water Oxidation

Yingxue Chang,[†] Nai-En Shi,[‡,§] Shulin Zhao,[†] Dongdong Xu,[†] Chunyan Liu,[†] Yu-Jia Tang,[†] Zhihui Dai,[†] Ya-Qian Lan,[†] Min Han,[*,†,§] and Jianchun Bao[*,†]

[†]Jiangsu Key Laboratory of Biofunctional Materials, School of Chemistry and Materials Science, Nanjing Normal University, Nanjing 210023, P. R. China

[‡]Key Laboratory for Organic Electronics and Information Displays, Institute of Advanced Materials, Nanjing University of Posts & Telecommunications, Nanjing 210023, P. R. China

[§]State Key Laboratory of Coordination Chemistry, Nanjing National Laboratory of Solid State Microstructures, Nanjing University, Nanjing 210093, P. R. China

Supporting Information

ABSTRACT: Core−shell nanohybrids containing cheap inorganic nanocrystals and nanocarbon shells are promising electrocatalysts for water splitting or other renewable energy options. Despite that great progress has been achieved, biomimetic synthesis of metal phosphates@nanocarbon core−shell nanohybrids remains a challenge, and their use for electrocatalytic oxygen evolution reaction (OER) has not been explored. In this paper, novel nanohybrids composed of coralloid $Co_2P_2O_7$ nanocrystal cores and thin porous nanocarbon shells are synthesized by combination of the structural merits of supramolecular polymer gels and a controllable thermal conversion technique, i.e., temperature programmable annealing of presynthesized supramolecular polymer gels that contain cobalt salt and phytic acid under a proper gas atmosphere. Electrocatalytic tests in alkaline solution show that such nanohybrids exhibit greatly enhanced electrocatalytic OER performance compared with that of $Co_2P_2O_7$ nanostructure. At a current density of 10 mA cm^{-2}, their overpotential is 0.397 V, which is much lower than that of $Co_2P_2O_7$ nanostructures, amorphous Co-Pi nanomaterials, $Co(PO_3)_2$ nanosheets, Pt/C, and some reported OER catalysts, and close to that of commercial IrO_2. Most importantly, both of their current density at the overpotential over 0.40 V and durability are superior to those of IrO_2 catalyst. As revealed by a series of spectroscopic and electrochemical analyses, their enhanced electrocatalytic performance results from the presence of thin porous nanocarbon shells, which not only improve interfacial electron penetration or transfer dynamics but also vary the coordination environment and increase the number of active 5-coordinated Co^{2+} sites in $Co_2P_2O_7$ cores.

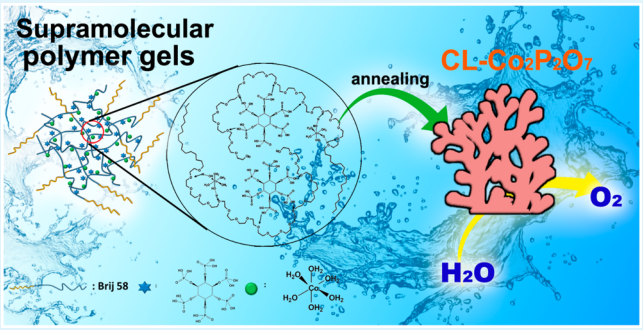

KEYWORDS: *core−shell nanostructures, cobalt phosphates, carbon, coordination environment and geometry, electrocatalysis, oxygen evolution reaction*

1. INTRODUCTION

The electrochemical and photochemical water splitting have been considered as two of the environmentally friendly approaches for energy storage and conversion, and production of clean H_2 fuels.[1−4] As for the electrochemical processes, the anodic oxygen evolution reaction (OER) is efficiency limiting due to the rigid O═O double bond formation and the sluggish proton-coupled electron transfer dynamics, and thus inhibits the large-scale application of electrochemical water splitting.[5−7] To resolve this problem, the key lies on finding highly efficient and robust OER catalysts to improve the kinetically slow process. Though noble-metal-based catalysts (e.g., RuO_2 and IrO_2) exhibit outstanding OER catalytic activity, their scarcity and high cost prohibit their practical use.[8,9] Inspired from photosynthetic system II that generates oxygen from water using Mn-based complex (Mn_4CaO_5) with an exceptionally high efficiency,[10] much efforts have been devoted to exploring alternative OER catalysts based on earth-abundant 3d transition metals (e.g., Mn, Fe, Co, Ni) and their derivatives.[11−19] Especially, Co-based materials, such as Co_3O_4 nanostructures and related nanohybrids,[20,21] Co_2O_3 nanoparticles,[22] amorphous or crystallized cobalt phosphate (Co-Pi) nanomaterials,[14,23,24] Co-Pi/α-Fe_2O_3 nanocomposites,[25] Co-based complexes,[26] vacancy-rich $NiCo_2O_4$ nanosheets,[27] Co-based chalcogenide nanosheets,[28] and so on, have been identified as promising OER catalysts because of their high catalytic activity

Received: June 15, 2016
Accepted: August 8, 2016
Published: August 8, 2016

DOI: 10.1021/acsami.6b07209
ACS Appl. Mater. Interfaces 2016, 8, 22534−22544

Scheme 1. Schematic Diagram for Formation of the Supramolecular Polymer Gels That Contain Cobalt Salt and Phytic Acid

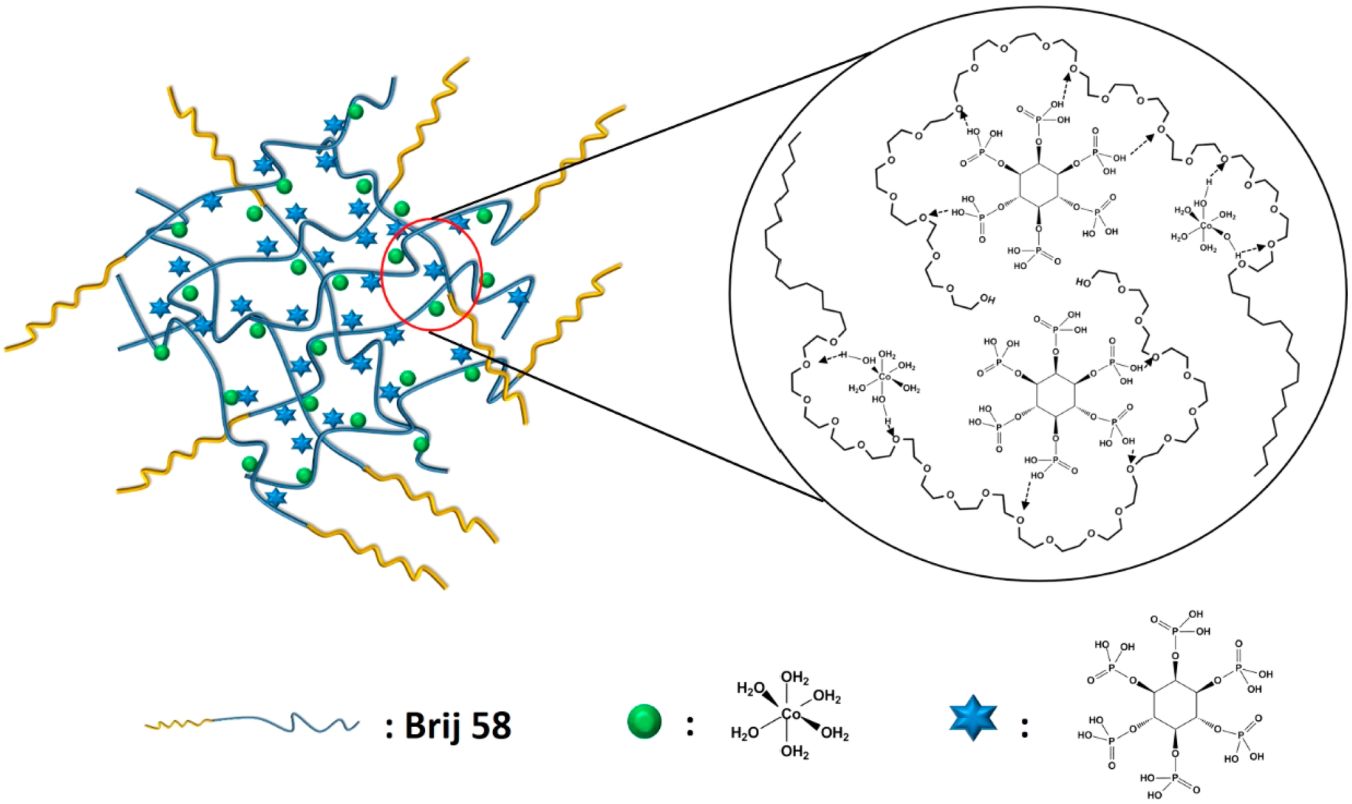

for water oxidation. Among those Co-based materials, most of them adopt the local octahedron (O_h) coordination of Co ions. Despite that the site geometries or coordination environment and related electronic structure of the transition metal greatly affect the catalytic activity,[11−13,15,16] there is still lack of systematic study on the correlation of the local Co coordination to OER catalysis. Additionally, the surface amorphization or activation has been often observed on most of the Co-based materials under typical pH and potential where the OER proceeds,[21,24,29] causing it to be hard to understand the OER mechanism and to develop new Co-based OER catalysts.

Transition metal phosphates offer positive contributions for structural stability and can adopt versatile structures with various positioning of the phosphate group.[30−32] Unlike common Co-based oxides that possess O_h coordination geometry of Co ions, phosphate/pyrophosphate-containing compounds show distinct Co-site geometries including tetrahedral, trigonal bipyramid, square pyramid, and O_h. Moreover, the flexible coordination of phosphate/pyrophosphate groups can endure the structural distortion by changing their local positions and stabilize the intermediate state of the transition metal ions.[33,34] For example, due to surface reconstruction induced by pyrophosphate ligands, $Na_2CoP_2O_7$ exhibits a highly distorted tetragonal site geometry of Co^{2+} ions, where H_2O molecules can favorably bind, resulting in a high OER activity comparable to that of amorphous Co-Pi and superior to that of $Li_2CoP_2O_7$, $NaCoPO_4$, and $LiCoPO_4$ materials.[35] These facts imply that varying coordination environment and site geometries can mediate the catalytic performance of desired OER catalysts. As a member of the Co-Pi materials family, $Co_2P_2O_7$ possesses unique optical, electrical, magnetic, and catalytic properties, showing great potential to use in coatings, Li-ion batteries, supercapacitors, magnetism and microwave absorption, as well as heterogeneous catalysis fields.[36−40] By far, some $Co_2P_2O_7$ nanostructures, such as nanoparticles, nanorods,[41] and hierarchical 3D nano/microarchitectures,[38,42] have been fabricated via different synthetic strategies. To the best of our knowledge, there is still no report on coralloid $Co_2P_2O_7$ nanocrystals or their derived nanohybrids, albeit great progress has been made in biomimetic nanostructures, and their OER activities are unknown until now. Considering that core−shell-type structures facilitate to boost a catalyst's performance,[43−45] and thin nanocarbon "envelopes" not only can enhance electrical conductivity and structural stability[46−49] but also may confine or mediate the coordination environment of the active components, designing novel nanohybrids composed of coralloid $Co_2P_2O_7$ nanocrystal cores and thin nanocarbon shells (CL-$Co_2P_2O_7$@C), and exploring their application toward OER, become an interesting topic. It is not only important for fundamental research but also for developing new Co-based OER catalysts to promote water oxidation and apply in many renewable energy options.

Herein, we report the synthesis of CL-$Co_2P_2O_7$@C core−shell nanohybrids and their electrocatalytic performance for OER. The typical synthesis is based on a facile two-step chemical route: (1) first, the special supramolecular polymer gels are prepared via a hydrogen-bonding and coordination-driven assembly strategy (Scheme 1), i.e., adding phytic acid into the aqueous solution of polyethylene glycol monocetyl ether (Brij 58) and $CoCl_2{\cdot}6H_2O$; (2) second, the supramolecular polymer gels are annealed in an oxygen-deficient or oxygen-rich atmosphere at different temperatures. At 750 °C under an Ar gas atmosphere, the desired CL-$Co_2P_2O_7$@C nanohybrids can be obtained, whereas, at 750 °C in an air atmosphere, the $Co(PO_3)_2$ nanosheets will be generated. As for

DOI: 10.1021/acsami.6b07209
ACS Appl. Mater. Interfaces 2016, 8, 22534−22544

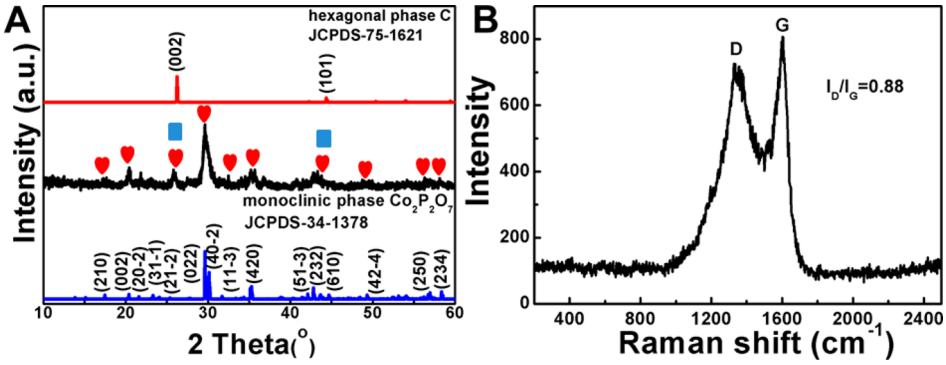

Figure 1. XRD pattern (A) and Raman spectrum (B) of the as-synthesized CL-$Co_2P_2O_7$@C core−shell nanohybrids.

CL-$Co_2P_2O_7$@C nanohybrids, their cores possess multiple branched nanounits that form zigzag chains and interleave into network-like or coralloid motifs, and their shells are thin nanocarbon layers with the average thickness of about 1.2−2 nm. Moreover, the nanocarbon shells are porous with the average pore size of about 4 nm. Such unique structural features not only facilitate to mass transfer but also may improve electron transfer dynamics, beneficial to electrocatalytic application for OER. Electrocatalytic tests in alkaline media reveal that such CL-$Co_2P_2O_7$@C nanohybrids exhibit much enhanced electrocatalytic OER performance compared with that of $Co_2P_2O_7$ nanostructures. At the current density of 10 mA cm^{-2}, their overpotential is 0.397 V, which is much lower than that of $Co_2P_2O_7$ nanostructures, amorphous Co-Pi nanomaterials, $Co(PO_3)_2$ nanosheets, Pt/C, and other reported OER catalysts (e.g., Au@Co_3O_4, mesoporous Co_3O_4, MnO_x, etc.), and close to that of commercial IrO_2. Most importantly, both the current density at the overpotential over 0.40 V and the durability of such nanohybrids are superior to those of IrO_2 catalyst. Moreover, on the basis of spectroscopic and electrochemical analysis, the possible origin of their excellent electrocatalytic performance is also suggested.

2. EXPERIMENTAL SECTION

2.1. Chemicals. Except for the special illustration, all chemical reagents used in this work were purchased from Alfa Aesar without further purification. The polyethylene glycol monocetyl ether (Brij 58, $HO(CH_2CH_2O)_{20}C_{16}H_{33}$, ~$M_n$ = 1124) was obtained from Tokyo Chemical Industry Co. Ltd. The commercial Pt/C (20%) and IrO_2 (99.9%) catalysts were bought from Alfa Aesar and Aladdin, respectively.

2.2. Synthesis of CL-$Co_2P_2O_7$@C Core−Shell Nanohybrids. In a typical synthesis, 5.6 g of Brij 58 was mixed with 7.3 g of deionized (DI) water under strong mechanical stirring for 1 h. Then, 10 mmol of $CoCl_2$ that was dissolved in 3.3 g of DI water was added into the above micelle system to form a uniform suspension. Subsequently, the suspension was heated to 80 °C and then cooled to room temperature. After repeatedly operating for three times, 2 mL of phytic acid was rapidly injected into the suspension at 80 °C and continuously stirred for 2 days. After naturally cooled down to room temperature and washed by a small amount of water, the product was collected, which was dried in vacuum at 50 °C for 2 h. Thus, the polymer gels that contain cobalt salt and phytic acid were obtained and used as precursors for annealing treatment. In a horizontal tube furnace, the presynthesized polymer gels were heated from room temperature to 750 °C under Ar gas with a heating rate of 2 °C min^{-1} and maintained at 750 °C for 2 h. After it cooled down to room temperature, the black product was collected and used for characterization.

2.3. Synthesis of $Co_2P_2O_7$ Nanostructures. For comparison, the $Co_2P_2O_7$ nanostructures were further obtained by exposing the CL-$Co_2P_2O_7$@C nanohybrids in air and retreating them at 750 °C for 2 h to oxidize and remove the carbon "envelope".

2.4. Synthesis of $Co(PO_3)_2$ Nanosheets. The synthesis of $Co(PO_3)_2$ nanosheets were similar to that for CL-$Co_2P_2O_7$@C nanohybrids. The only difference was that the obtained polymer gels were directly annealed at 750 °C in air.

2.5. Materials Characterization. The X-ray diffraction (XRD) patterns were collected on a D/max 2500 VL/PC diffractometer (Japan) equipped with graphite monochromatized Cu Kα radiation (λ = 1.54060 Å). The Raman spectra were recorded on a JY HR 800 (France) instrument with an optical multichannel spectrometer Microdil 28 (Dilor) equipped with a microscope. An objective with 100× magnification was used both for focusing the excitation light (Ar^+ laser, 488 nm) and for collecting the scattered light. The transmission electron microscopy (TEM) images were carried out on JEOL-2100F and FEI, Talos F200X apparatuses at the accelerating voltage of 200 kV, which are equipped with STEM and EDS detectors that can be used for elemental mapping analysis. The X-ray photoelectron spectra (XPS) were recorded on a scanning X-ray microprobe (PHI 5000 Versa, ULACPHI, Inc.) that uses Al Kα radiation. The binding energy of the C 1s peak (284.6 eV) was employed as a standard to calibrate the binding energies of other elements. As for the electrochemical impedance spectra, they were carried out on a BioLogic SP-150 electrochemical workstation. The diffuse reflectance spectra measurements were performed on a Shimadzu UV−vis−NIR spectrometer (UV-3600) by using spectroscopically pure $BaSO_4$ as the reference sample. The optical spectra were recorded in the range of 5000−50 000 cm^{-1}. According to the Kubelka−Munk approximation, the remission function $F(R)$ was defined as follows: $F(R) = K/S = (1 - R)^2/2R$, where K and S are the absorption and scattering coefficient, respectively, and R is the limiting reflectance.

2.6. Electrocatalytic Measurements. The electrocatalytic tests were carried out on the CHI 700e workstation equipped with a Gamry's Rotating Disk Electrode (RDE). The diameter of the RDE is 5 mm. For all the tests, a standard three-electrode system was adopted. The Ag/AgCl and Pt foil were used as the reference and counter electrodes, respectively. The catalysts modified RDE were used as the working electrodes, which were fabricated as follows: 4 mg of CL-$Co_2P_2O_7$@C nanohybrids or other control samples were dispersed in 2 mL of ethanol and water ($V_{ethanol}$:V_{water} = 1:3) to generate a uniform catalyst ink. A 20 μL aliquot of such catalyst ink was dropped onto pretreated RDE using a microliter syringe. After drying, 5 μL of 1.0 wt % Nafion solution was added. Thus, the catalysts modified RDE were fabricated. In the OER tests, the polarization curves were recorded at the potential window of 0−1.0 V (vs Ag/AgCl) with the electrode rotation rate of 1600 rpm, and these polarization curves were corrected for solution resistance. The resistance of 0.1 M KOH is ~42 Ω, as revealed by the iR compensation function of the electrochemical workstation.

For comparison, all potentials were converted to reversible hydrogen electrode (RHE) values. The detailed calibration process was carried out according to a previous report.[50] In this work, the

DOI: 10.1021/acsami.6b07209
ACS Appl. Mater. Interfaces 2016, 8, 22534−22544

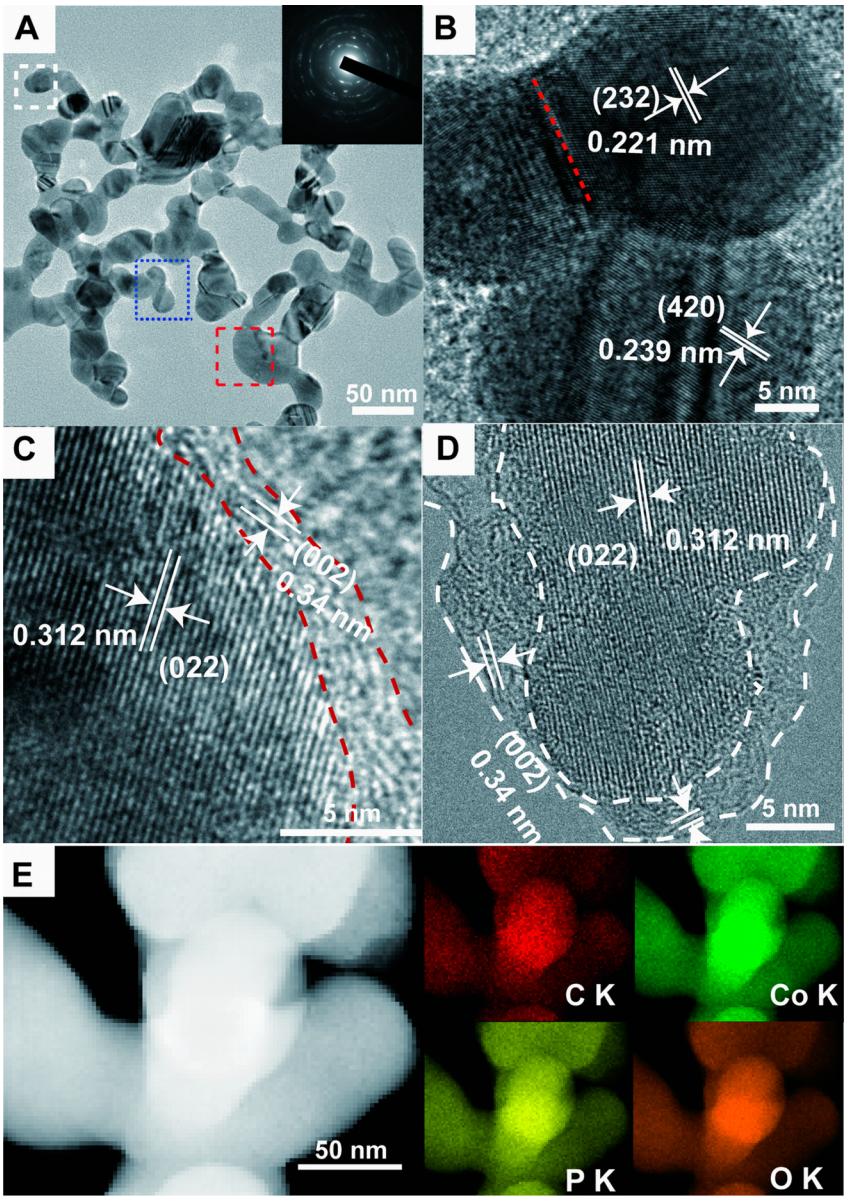

Figure 2. (A) Low-magnification TEM image of the CL-$Co_2P_2O_7$@C core−shell nanohybrids. The inset shows the related SAED pattern. (B) HRTEM image of an individual triple-branched $Co_2P_2O_7$@C nanounit indicated by the blue rectangular frame in (A). (C) HRTEM image of another $Co_2P_2O_7$@C nanounit marked by the red rectangular frame in (A). (D) HRTEM image of another $Co_2P_2O_7$@C nanounit marked by the white rectangular frame in (A). (E) HAADF-STEM and element-mapping images of a magnified branched region in CL-$Co_2P_2O_7$@C nanohybrids.

formula, E (RHE) = E (Ag/AgCl) + 0.973 V, was used for calibrating the work potential with reference to RHE.

3. RESULTS AND DISCUSSION

The composition and crystallinity of the as-synthesized CL-$Co_2P_2O_7$@C core−shell nanohybrids were identified by powder X-ray diffraction (XRD) and Raman spectrum. The corresponding XRD pattern is shown in Figure 1A. At the 2θ ranging from 10° to 60°, 10 obvious diffraction peaks that are marked with a red heart are observed, which can be indexed to (210), (002), (21$\bar{2}$), (022), (11$\bar{3}$), (420), (232), (424), (250), and (234) planes of $Co_2P_2O_7$ with a monoclinic phase structure (JCPDS No. 34-1378). The diffraction peaks at the 2θ of 26° and 43.5° that are indicated by a blue square are assigned to the (002) and (101) planes of hexagonal graphite, which are overlapped with those of (21$\bar{2}$) and (232) planes of monoclinic phase $Co_2P_2O_7$. The Raman spectrum shown in Figure 1B further confirms the existence of the carbon nanostructures component in the obtained nanohybrids. The peaks at 1359 and 1598 cm^{-1} are attributed to the D- (sp^3-hybridized C) and G- (sp^2-hybridized C) bands of graphitized carbon nanostructures. The intensity ratio of D- and G-peaks (I_D/I_G) is calculated to be about 0.88 (based on the peak height ratio), revealing that there are large amounts of sp^3-hybridized C for the carbon nanostructures component in the obtained nanohybrids.

The shape and microstructure of the CL-$Co_2P_2O_7$@C nanohybrids were further examined by transmission electron microscopy (TEM) and N_2 adsorption−desorption test. From the low-magnification TEM image (Figure 2A), the obvious coralloid nanostructures with irregular branches or protuberances can be observed. Some branches or protuberances are interconnected to form zigzag chains, which show the clear grain boundaries between the units of each chain. The formed

DOI: 10.1021/acsami.6b07209
ACS Appl. Mater. Interfaces 2016, 8, 22534−22544

zigzag chains are interleaved to form network-like or coralloid motifs. Moreover, the moiré fringes can be seen on some protuberances, implying that they may be fused by the small nanocrystals. The selected area electron diffraction (SAED) pattern (inset of Figure 2A) exhibits clear concentric rings, revealing that they are polycrystalline. Figure 2B gives the related high-resolution TEM image of an individual triple-branched $Co_2P_2O_7$@C nanohybrid indicated by the blue rectangular frame in Figure 2A. Besides the interfaces and dislocation or defects among those branches, the clear lattice fringes with the spacing of 2.21 and 2.39 Å are observed, corresponding to the (232) and (420) planes of monoclinic phase $Co_2P_2O_7$, respectively. No obvious carbon shells are observed on each branch of this selected nanounit, implying that the carbon shells are very thin or maybe in monolayer form (just like graphene). To identify the existence of the carbon shells, we select the edge area of another branch nanounit marked by the red rectangular frame in Figure 2A and another branch nanounit as the white rectangular frame indicated in Figure 2A to make the HRTEM analysis. As illustrated in Figure 2C,D, except for the lattice fringes for $Co_2P_2O_7$ (3.12 Å), the obvious lattice fringes with the spacing of ~3.40 Å are observed on the envelope of the $Co_2P_2O_7$ core, which is attributed to the (002) plane of hexagonal graphite. These results confirm the presence of carbon shells on the CL-$Co_2P_2O_7$ nanocrystals, but their thickness is not uniform. Other representative HRTEM images where one can see thinner carbon shells are given in the Supporting Information (SI) (Figure S1A−C). By statistical analysis of 100 branched nanounits, the average thickness of the carbon shells is found to be about 1.2−2 nm. Such thin carbon shells not only can "armor" the CL-$Co_2P_2O_7$ cores and alleviate their destruction under electrochemical cycling but also may enhance the electron penetration or tunneling, facilitating electrocatalytic application according to previous reports on carbon nanostructures wrapping metal or other inorganic nanoparticles hybrids.[51,52] Further high-angle annular dark-field scanning transmission electron microscopy (HAADF-STEM) and element-mapping images (Figure S1D and Figure 2D) verify that C, Co, P, and O elements are homogeneously distributed along the CL-$Co_2P_2O_7$@C nanohybrids. The related N_2 adsorption−desorption test results (Figure S2) reveal that such nanohybrids possess a mesoporous structure with a BET surface area of 33 m^2 g^{-1} and the average pore size of about 4 nm. Combined with HRTEM analysis (the $Co_2P_2O_7$ cores are solid, not hollow or porous), the mesopores may result from the carbon "envelope", which could be helpful for the reactants to contact with inner $Co_2P_2O_7$ cores for triggering and promoting the desired catalytic reaction.

To get an insight on the growth mechanism of the CL-$Co_2P_2O_7$@C nanohybrids, a series of control experiments were carried out. The impact factors, including the annealing temperature and annealing environment, are systematically studied. Under an oxygen-deficient environment (Ar gas), the presynthesized supramolecular polymer gels are annealed at 400, 550, 750, and 900 °C, respectively, and the obtained products are characterized by TEM, XRD, and XPS. At 400 °C, the network-like structure that was intervolved by amorphous cobalt phosphate nanofibers (Co-Pi-1) is generated (Figure S3). As the annealing temperature is raised to 550 °C, the large-area fishing-net-like structures composed of amorphous cobalt phosphate nanochains with large diameters (Co-Pi-2) will be produced (Figure S4). At 750 °C, the original interconnected network-like nanostructures are partially fractured and converted into CL-$Co_2P_2O_7$@C nanohybrids. When the temperature is further increased to 900 °C, the mixed phase product of $Co_2P_2O_7$, CoP, and C with thin-sheet-like motifs will be obtained (Figure S5). While under an oxygen-rich environment (in air), the network-like structures can be reserved as the gel-like precursors are annealed at 400 °C (Figure S6A,B), but they are also amorphous cobalt phosphate (Co-Pi-3). Under this environment, by increasing the annealing temperature, the amorphous sheet-like or layer-like cobalt phosphate nanostructures (Co-Pi-4) are formed at 550 °C (Figure S6C,D), and the crystallized sheet-like $Co(PO_3)_2$ nanostructures will be generated at 750 °C (Figure S7A,B). The corresponding HRTEM image and Raman spectrum confirm that there are no nanocarbon shells present on $Co(PO_3)_2$ nanosheets (Figure S7C,D). These facts indicate that both the annealing temperature and the annealing environment affect the composition, crystallinity, and morphology of the final product. Under the oxygen-deficient environment, the polymer chains are hard to be removed with the increase of annealing temperature, which will be gradually carbonized and provide a confined space to assist the combination of cobalt and phosphor resources and allow the product to farthest inherit the morphology of the gel precursors. On the contrary, in an oxygen-rich atmosphere, the polymer chains will be gradually removed by oxidation with the raising of annealing temperature, which will let the rapid fusion of cobalt and phosphor precursors that is difficult to preserve the shape of the gel precursors. On the basis of those results, the plausible process for formation of CL-$Co_2P_2O_7$@C nanohybrids is given in Scheme 2.

Scheme 2. Schematic Process for the Formation of CL-$Co_2P_2O_7$@C Nanohybrids

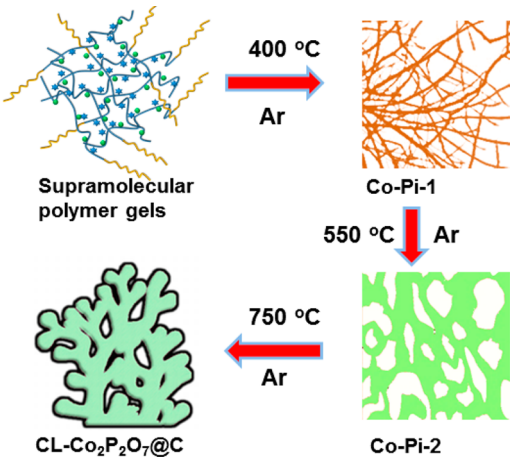

The electrocatalytic properties of the CL-$Co_2P_2O_7$@C nanohybrids were evaluated in 0.1 M KOH electrolyte by using OER as the probe reaction. In view of previous reports that amorphous Co-Pi and Co-Fe-O materials possess much higher OER activities than their crystalline counterparts,[14,24,53] the OER activity of CL-$Co_2P_2O_7$@C nanohybrids is first compared with that of amorphous Co-Pi-1, Co-Pi-2, Co-Pi-3, and Co-Pi-4 (Figure S8). The results demonstrate that the nanohybrids outperform the four amorphous Co-Pi nanomaterials. This "abnormal" phenomenon may result from the presence of a carbon "armor" in our core−shell nanohybrids,

DOI: 10.1021/acsami.6b07209
ACS Appl. Mater. Interfaces 2016, 8, 22534−22544

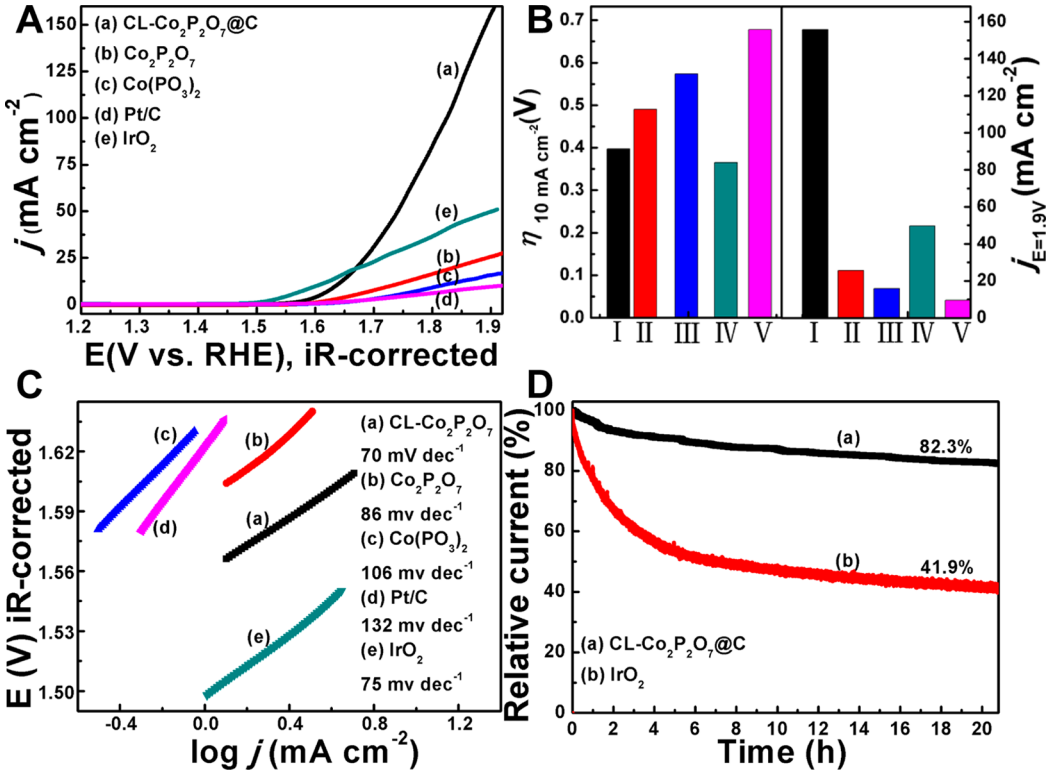

Figure 3. (A) OER polarization plots for CL-$Co_2P_2O_7$@C nanohybrids (a), $Co_2P_2O_7$ nanostructures (b), $Co(PO_3)_2$ nanosheets (c), Pt/C (d), and IrO_2 (e) catalysts. (B) Comparison of the OER overpotential at a current density of 10 mA cm^{-2} and the current density at 1.9 V (vs RHE) for CL-$Co_2P_2O_7$@C nanohybrids (I), $Co_2P_2O_7$ nanostructures (II), $Co(PO_3)_2$ nanosheets (III), IrO_2 (IV), and Pt/C (V) catalysts. (C) Related Tafel plots for those catalysts. (D) Chronoamperometric plots for CL-$Co_2P_2O_7$@C nanohybrids (a) and IrO_2 catalyst (b) at 1.7 V (vs RHE).

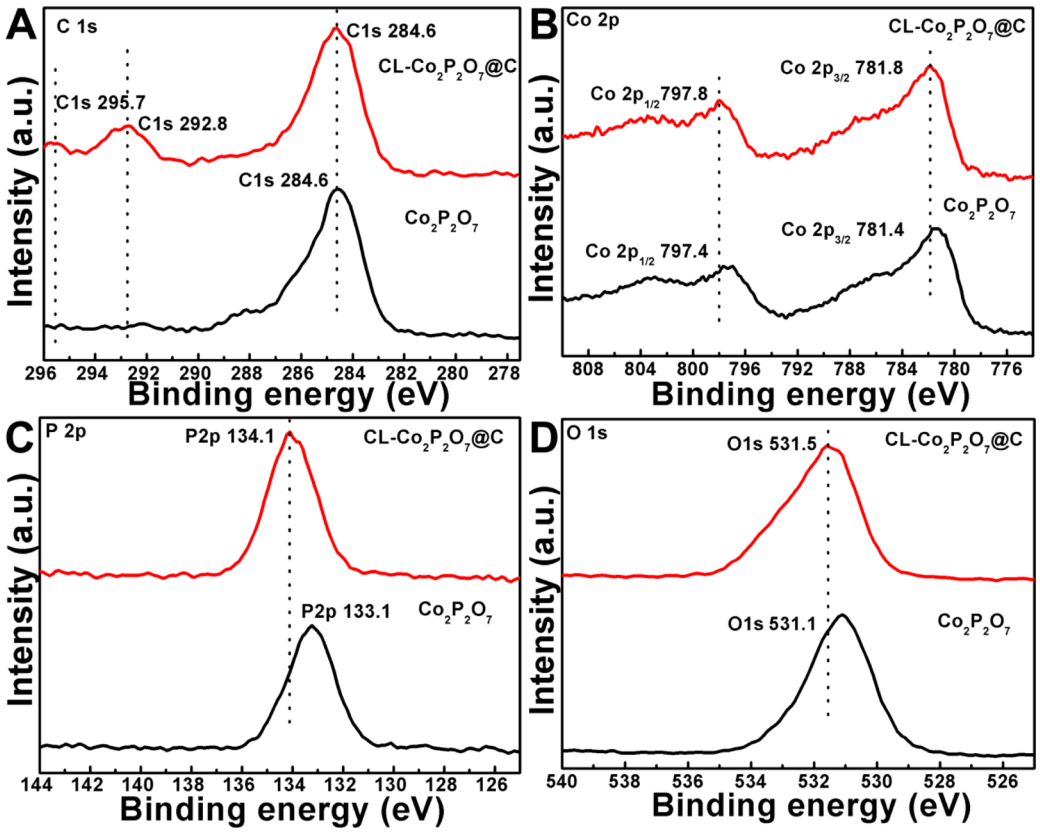

Figure 4. Comparison of (A) C 1s, (B) Co 2p, (C) P 2p, and (D) O 1s core level XPS spectra for CL-$Co_2P_2O_7$@C nanohybrids and $Co_2P_2O_7$ nanostructures.

DOI: 10.1021/acsami.6b07209
ACS Appl. Mater. Interfaces 2016, 8, 22534−22544

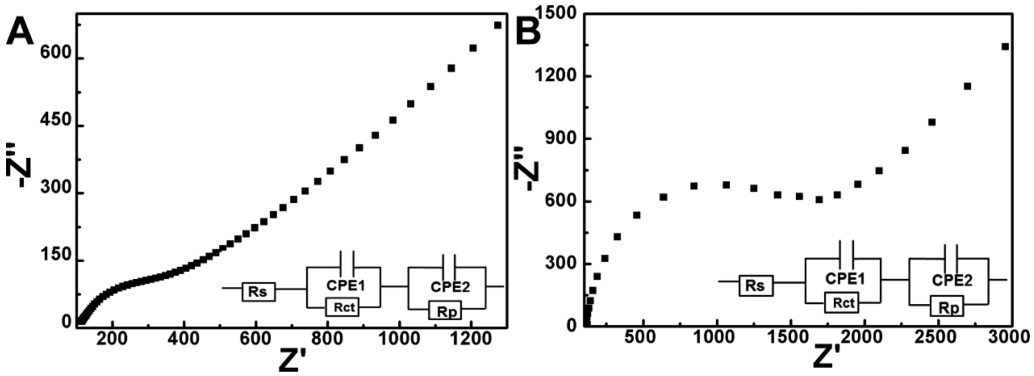

Figure 5. (A) EIS spectrum and equivalent circuit for CL-$Co_2P_2O_7$@C nanohybrids. (B) EIS spectrum and equivalent circuit for $Co_2P_2O_7$ nanostructures.

which can suppress surface amorphism and enhance the coupling or synergistic effect with the crystallined $Co_2P_2O_7$ core. To further examine the OER activity of our nanohybrids, the crystallined Co-Pi materials including $Co_2P_2O_7$ nanostructures (Figure S9) and $Co(PO_3)_2$ nanosheets, and commercial Pt/C and IrO_2 are used as the control catalysts yet. Figure 3A shows the OER polarization plots of those five crystallined catalysts at the potential window of 1.2−1.9 V (vs RHE). From the magnified OER polarization curves (Figure S10), the onset oxidation potential of the CL-$Co_2P_2O_7$@C nanohybrids is identified to be 1.37 V (vs RHE). In 0.1 M KOH electrolyte (pH = 13), the overpotential (η) for OER can be calculated according to the formula: $\eta = E$(V vs RHE) − 1.238 V. Thus, the onset overpotential of CL-$Co_2P_2O_7$@C nanohybrids is calculated to be about 0.132 V, which is smaller than that of $Co_2P_2O_7$ nanostructures (0.272 V), $Co(PO_3)_2$ nanosheets (0.362 V), Pt/C (0.312 V), and IrO_2 (0.212 V) catalysts. Except for onset overpotential, the overpotential at a current density of 10 mA cm^{-2} ($\eta_{10\ mA\ cm^{-2}}$) is a key benchmark for evaluating the electrocatalytic performance of a desired OER catalyst.[54] As illustrated in Figure 3B, the $\eta_{10\ mA\ cm^{-2}}$ of CL-$Co_2P_2O_7$@C nanohybrids is about 0.397 V, which is close to that of IrO_2 (0.365 V) and $NiCoO_x$ film,[55] but much smaller than that of $Co_2P_2O_7$ nanostructures (0.490 V), $Co(PO_3)_2$ nanosheets (0.574 V), Pt/C (0.678 V), and some recently reported OER catalysts, such as ordered mesoporous Co_3O_4 (0.525 V),[56] acidically oxidized carbon cloth (0.477 V),[57] Ni@$[Ni_{(2+/3+)}Co_2(OH)_{6-7}]_x$ nanotubes (0.460 V),[58] amorphous Co-Fe-O film (0.442 V),[53] Co_3S_4/N-doped CNTs (0.430 V),[59] Au@Co_3O_4 (0.420 V),[60] and so on. Except for $\eta_{10\ mA\ cm^{-2}}$, the current densities at 1.9 V (vs RHE) ($j_{E=1.90\ V}$) are also compared and listed in Figure 3B. It is clear that the $j_{E=1.9\ V}$ on CL-$Co_2P_2O_7$@C nanohybrids can reach 155.7 mA cm^{-2}, which is 6, 10, 16, and 3 times as high as that of $Co_2P_2O_7$ nanostructures (25.6 mA cm^{-2}), $Co(PO_3)_2$ nanosheets (15.8 mA cm^{-2}), Pt/C (9.5 mA cm^{-2}), and IrO_2 (49.8 mA cm^{-2}), respectively. Additionally, to evaluate the OER kinetics of those catalysts, the related Tafel plots (η−log j) are obtained (Figure 3C). On the basis of the calculated Tafel slope values, the OER kinetics of CL-$Co_2P_2O_7$@C nanohybrids is close to that of IrO_2 while superior to that of $Co_2P_2O_7$ nanostructures, $Co(PO_3)_2$ nanosheets, and Pt/C catalyst.

In addition, the long-term stability or durability is another important standard to examine the application prospect of a specific electrocatalyst.[61] The durability tests for CL-$Co_2P_2O_7$@C nanohybrids are further performed by using the chronopotentiometry method at a constant potential of 1.7 V (vs RHE). As illustrated in Figure 3D, 82.3% of the initial current density can be reserved on CL-$Co_2P_2O_7$@C nanohybrids after continuously cycling for 75 000 s, whereas, for commercial IrO_2 catalyst, only 41.9% of initial current density can be retained under the same test conditions. This result implies that the durability of the former is better than that of the latter.

To tentatively understand the good catalytic performance of the CL-$Co_2P_2O_7$@C nanohybrids, XPS was first used to characterize their surface chemical and electronic structure. The related survey XPS spectrum is given in Figure S11A. As shown in Figure 4A, the C 1s core level spectrum reveals that the surface of the C shell layer is partially oxidized with the formation of −C−O, −C═O, O═C−O−P− bonds on the CL-$Co_2P_2O_7$@C nanohybrids. The detailed deconvolution of C 1s peaks is shown in Figure S11B. Compared with that of $Co_2P_2O_7$ nanostructures (actually containing a trace amount of residual carbon), the binding energy (BE) of C 1s for CL-$Co_2P_2O_7$@C nanohybrids is slightly negatively shifted to the low-energy direction. For Co 2p (Figure 4B), P 2p (Figure 4C), and O 1s (Figure 4D) core level spectra, they confirm that the oxidation states of Co, P, and O elements are +2, + 5, and −2 (see Figure S11C−E for the detailed discussion), respectively. Moreover, relative to that of $Co_2P_2O_7$ nanostructures (the details, please see Figure S11F−J), the BEs of Co 2p, P 2p, and O 1s for CL-$Co_2P_2O_7$@C nanohybrids are largely shifted to the high-energy direction, implying that there is a strong electronic coupling effect between the two components, and the electrons may transfer from the $Co_2P_2O_7$ cores to thin C shells. In other words, the thin C shells can enhance electron penetration or interfacial electron transfer. Further evidence comes from the electrochemical impedance spectrum (EIS) tests. From the Nyquist plot and equivalent circuit (Figure 5A) of CL-$Co_2P_2O_7$@C nanohybrids, their interfacial electron transfer resistance (R_{ct}) is identified to be 55 Ω, which is much smaller than that of $Co_2P_2O_7$ nanostructures (Figure 5B, R_{ct} = 1066 Ω). This result confirms that the interfacial electron transfer dynamics of CL-$Co_2P_2O_7$@C nanohybrids is much faster than that of $Co_2P_2O_7$ nanostructures.

Besides increasing electrical conductivity and improving interfacial electron transfer dynamics, do the thin C shells play another important role? As we know, the variation of coordination environment will change the coordination geometry or symmetry of central transition metal ions,[35] which may affect the number of catalytic active sites. For Co^{2+}, the 5-coordinated geometry with C_{4v} or D_{3h} symmetry is more active than 6-coordinated geometry with O_h symmetry. According to the previous spectrum study, the bulk $Co_2P_2O_7$

DOI: 10.1021/acsami.6b07209
ACS Appl. Mater. Interfaces 2016, 8, 22534−22544

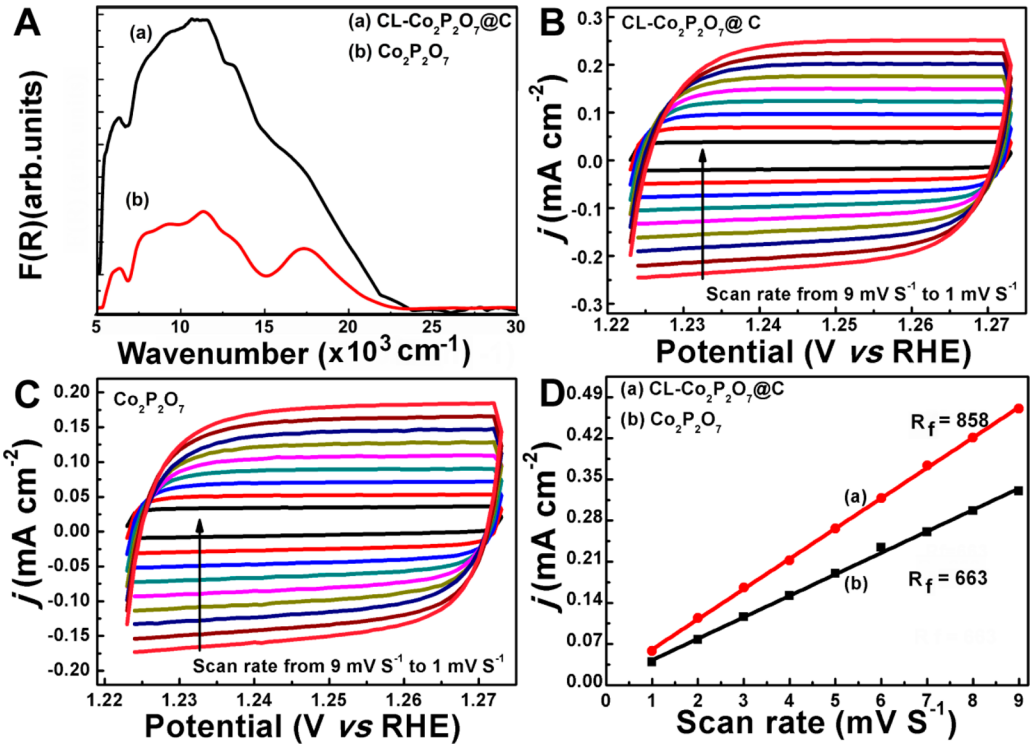

Figure 6. (A) Diffuse reflectance spectra of (a) CL-$Co_2P_2O_7$@C nanohybrids, and (b) $Co_2P_2O_7$ nanostructures. (B, C) Cyclic voltammograms of the CL-$Co_2P_2O_7$@C nanohybrids (B) and $Co_2P_2O_7$ nanostructures (C) electrodes in the low potential region at various scan rates (1−9 mV s^{-1}). (D) Current density as a function of the scan rate for CL-$Co_2P_2O_7$@C nanohybrids (a) and $Co_2P_2O_7$ nanostructures (b) electrodes.

powder possesses 5- and 6-coordinated Co^{2+} with C_{4v} and O_h symmetry, respectively.[62] In the CL-$Co_2P_2O_7$@C nanohybrids, the thin C shells not only facilitate to form and sustain the coralloid geometry of $Co_2P_2O_7$ cores but also change their coordination environment, which may increase the number of active 5-coordinated Co^{2+} sites. The corresponding optical spectrum tests confirm this viewpoint. Figure 6A presents the remission functions $F(R)$ obtained from the diffuse reflectance spectra of CL-$Co_2P_2O_7$@C nanohybrids and $Co_2P_2O_7$ nanostructures. The spectra show the bands with different intensities arising from Co^{2+} solely. Two main transitions can be distinguished in those two kinds of $Co_2P_2O_7$ nanostructures: one is in the NIR region with relatively high intensities, and the other is in the visible region with lower intensities. In the NIR region, the bands at about 6250 and 11 500 cm^{-1} are attributed to the energy levels of $^4E(F)$ and $^4B_1(F)$ for 5-coordinated Co^{2+} with C_{4v} symmetry, and the band at about 8100 cm^{-1} can be assigned to the $^4T_{1g}(F)$ to $^4T_{2g}(F)$ transition for 6-coordinated Co^{2+} in O_h symmetry according to a previous report.[63] As for the visible region, the band at 17 400 cm^{-1} is attributed to the energy level of $^4E(P)$ for 5-coordinated Co^{2+} with C_{4v} symmetry, and the shoulder band at about 19 100 cm^{-1} originates from the transition of $^4T_{1g}(F)$ to $^4T_{1g}(P)$ energy level for 6-coordinated Co^{2+} with O_h symmetry.[62,63] Obviously, the intensities of all the bands for 5-coordianted Co^{2+} in CL-$Co_2P_2O_7$@C nanohybrids are much higher than those of $Co_2P_2O_7$ nanostructures, implying that there are many 5-coordinated Co^{2+} sites in the former sample. That is to say, the thin C shells can vary the coordination geometry of $Co_2P_2O_7$ cores and greatly increase the number of active 5-coordinated Co^{2+} sites yet. To further verify the correlation of the thin C shells and the number of active sites, the capacitance of the catalyst−solution interface and the roughness factors of the two $Co_2P_2O_7$ samples with or without C shells were estimated. As shown in Figure 6B,C, the current densities were measured from 1 to 9 mV s^{-1} at 1.232 V (vs RHE) and can be plotted as a function of scan rate (Figure 6D) to study the effective surface area of the $Co_2P_2O_7$ samples by evaluating the electrochemical double-layer capacitance (C_{dl}) and the roughness factor (R_f). Calculated from Figure 6D, the C_{dl} and R_f for the CL-$Co_2P_2O_7$@ C nanohybrids are 51.5 mF cm^{-2} and 858, respectively, which are much higher than those of $Co_2P_2O_7$ nanostructures (C_{dl} = 39.8 mF cm^{-2}, R_f = 663). The much higher C_{dl} and R_f values of the nanohybrids reveal that there are much or more effective active sites on them, consistent with optical spectrum analysis.

4. CONCLUSIONS

In summary, the CL-$Co_2P_2O_7$@C core−shell nanohybrids have been synthesized for the first time by controllable annealing of presynthesized supramolecular polymer gels that contain cobalt salt and phytic acid at the proper temperature and gas atmosphere. Both Raman and HRTEM analyses confirm the existence of thin C shells, whose average thickness is about 1.2−2.0 nm by statistical analysis from HRTEM images. Related N_2 adsorption−desorption test discloses that the carbon shells are mesoporous structures with the average pore size of about 4 nm. After exposing the nanohybrids in air at 750 °C, the thin C shells can be removed, but the morphology of the $Co_2P_2O_7$ cores will be destroyed accordingly, implying that the two constituents are well-coupled and the C shells are a good "armor" for the CL-$Co_2P_2O_7$ cores. Such nanohybrids exhibit much enhanced electrocatalytic OER performances in alkaline media compared with that of $Co_2P_2O_7$ nanostructures. At a current density of 10 mA cm^{-2}, their overpotential is 0.397 V, which is much lower

DOI: 10.1021/acsami.6b07209
ACS Appl. Mater. Interfaces 2016, 8, 22534−22544

than that of $Co_2P_2O_7$ nanostructures, amorphous Co-Pi materials, $Co(PO_3)_2$ nanosheets, Pt/C, and some recently reported OER electrocatalysts (e.g., Au@Co_3O_4, mesoporous Co_3O_4, MnO_x, etc.), and close to that of commerical IrO_2. As the overpotential surpasses 0.40 V, the current density of such nanohybrids is drastically increased, outperforming the IrO_2 catalyst. Most importantly, their durability is superior to that of IrO_2 yet. On the basis of a series of spectroscopic and electrochemical analysis, their excellent electrocatalytic performance originates from the presence of thin porous nanocarbon shells, which not only enhance electron penetration or interfacial electron transfer dynamics but also mediate the coordination geometry of $Co_2P_2O_7$ cores and increases the number of active 5-coordinated Co^{2+} sites. This work not only develops a supramolecular polymer gel chemical route to prepare novel biomimetic core−shell nanohybrids but also paves the way for rational design of a cheap and robust OER catalyst to apply in water splitting or other renewable energy fields.

■ ASSOCIATED CONTENT

Supporting Information

The Supporting Information is available free of charge on the ACS Publications website at DOI: 10.1021/acsami.6b07209.

Other typical HRTEM images and mapping figures as well as N_2 adsorption−desorption test data of CL-$Co_2P_2O_7$@C nanohybrids (Figures S1 and S2), characterization of the samples obtained by annealing polymer gels at 400−900 °C in Ar and air atmospheres (Figures S3−S8), characterization of $Co_2P_2O_7$ nanostructures (Figure S9), and additional electrochemical and spectroscopic data for CL-$Co_2P_2O_7$@C nanohybrids (Figures S10−S12) (PDF)

■ AUTHOR INFORMATION

Corresponding Authors

*Phone: 86-25-85891051. Fax: +86-25-85891051. E-mail: 07203@njnu.edu.cn (M.H.).

*E-mail: baojianchun@njnu.edu.cn (J.B.).

Author Contributions

[‖]The manuscript was written through contributions of all authors. All authors have given approval to the final version of the manuscript. Y. Chang, N.-E. Shi, and S. Zhao contributed equally.

Notes

The authors declare no competing financial interest.

■ ACKNOWLEDGMENTS

We greatly appreciate the financial support from the National Natural Science Foundation of China under the projects (Nos. 21271105, 21541007, 21471082, 21475062, and 21471081), and research fund from the Priority Academic Program Development of Jiangsu Higher Education Institutions as well as the opening research foundation from the State Key Laboratory of Coordination Chemistry, Nanjing National Laboratory of Solid State Microstructures, Nanjing University.

■ REFERENCES

(1) Gust, D.; Moore, T. A.; Moore, A. L. Solar Fuels *via* Artificial Photosynthesis. *Acc. Chem. Res.* **2009**, *42*, 1890−1898.

(2) Swierk, J. R.; Mallouk, T. E. Design and Development of Photoanodes for Water-Splitting Dye-sensitized Photoelectrochemical Cells. *Chem. Soc. Rev.* **2013**, *42*, 2357−2387.

(3) Jiao, Y.; Zheng, Y.; Jaroniec, M.; Qiao, S. Z. Design of Electrocatalysts for Oxygen- and Hydrogen-Involving Energy Conversion Reactions. *Chem. Soc. Rev.* **2015**, *44*, 2060−2086.

(4) Li, J.; Wang, Y.; Zhou, T.; Zhang, H.; Sun, X.; Tang, J.; Zhang, L.; Al-Enizi, A. M.; Yang, Z.; Zheng, G. Nanoparticle Superlattices as Efficient Bifunctional Electrocatalysts for Water Splitting. *J. Am. Chem. Soc.* **2015**, *137*, 14305−14312.

(5) Suntivich, J.; May, K. J.; Gasteiger, H. A.; Goodenough, J. B.; Shao-Horn, Y. A Perovskite Oxide Optimized for Oxygen Evolution Catalysis from Molecular Orbital Principles. *Science* **2011**, *334*, 1383−1385.

(6) Lee, S. W.; Carlton, C.; Risch, M.; Surendranath, Y.; Chen, S.; Furutsuki, S.; Yamada, A.; Nocera, D. G.; Shao-Horn, Y. The Nature of Lithium Battery Materials under Oxygen Evolution Reaction Conditions. *J. Am. Chem. Soc.* **2012**, *134*, 16959−16962.

(7) Wang, J.; Zhong, H. X.; Qin, Y. L.; Zhang, X. B. An Efficient Three-Dimensional Oxygen Evolution Electrode. *Angew. Chem., Int. Ed.* **2013**, *52*, 5248−5253.

(8) Sun, Y.; Gao, S.; Lei, F.; Liu, J.; Liang, L.; Xie, Y. Atomically-Thin Non-layered Cobalt Oxide Porous Sheets for Highly Efficient Oxygen-Evolving Electrocatalysts. *Chem. Sci.* **2014**, *5*, 3976−3982.

(9) Wang, Y.; Zhou, T.; Jiang, K.; Da, P.; Peng, Z.; Tang, J.; Kong, B.; Cai, W.-B.; Yang, Z.; Zheng, G. Reduced Mesoporous Co_3O_4 Nanowires as Efficient Water Oxidation Electrocatalysts and Supercapacitor Electrodes. *Adv. Energy Mater.* **2014**, *4*, 1400696.

(10) Umena, Y.; Kawakami, K.; Shen, J. -R; Kamiya, N. Crystal Structure of Oxygen-Evolving Photosystem II at a Resolution of 1.9 Å. *Nature* **2011**, *473*, 55−60.

(11) Bergmann, A.; Zaharieva, I.; Dau, H.; Strasser, P. Electrochemical Water Splitting by Layered and 3D Cross-Linked Manganese Oxides: Correlating Structural Motifs and Catalytic Activity. *Energy Environ. Sci.* **2013**, *6*, 2745−2755.

(12) Park, J.; Kim, H.; Jin, K.; Lee, B. J.; Park, Y.-S.; Kim, H.; Park, I.; Yang, K. D.; Jeong, H.-Y.; Kim, J.; Hong, K. T.; Jang, H. W.; Kang, K.; Nam, K. T. A New Water Oxidation Catalyst: Lithium Manganese Pyrophosphate with Tunable Mn Valency. *J. Am. Chem. Soc.* **2014**, *136*, 4201−4211.

(13) Friebel, D.; Louie, M. W.; Bajdich, M.; Sanwald, K. E.; Cai, Y.; Wise, A. M.; Cheng, M.-J.; Sokaras, D.; Weng, T.-C.; Alonso-Mori, R.; Davis, R. C.; Bargar, J. R.; Nørskov, J. K.; Nilsson, A.; Bell, A. T. Identification of Highly Active Fe Sites in (Ni, Fe)OOH for Electrocatalytic Water Splitting. *J. Am. Chem. Soc.* **2015**, *137*, 1305−1313.

(14) Kanan, M. W.; Nocera, D. G. In Situ Formation of an Oxygen-Evolving Catalyst in Neutral Water Containing Phosphate and Co^{2+}. *Science* **2008**, *321*, 1072−1075.

(15) Grimaud, A.; May, K. J.; Carlton, C. E.; Lee, Y.-L.; Risch, M.; Hong, W. T.; Zhou, J.; Shao-Horn, Y. Double Perovskites as a Family of Highly Active Catalysts for Oxygen Evolution in Alkaline Solution. *Nat. Commun.* **2013**, *4*, 2439.

(16) Song, F.; Hu, X. Ultrathin Cobalt-Manganese Layered Double Hydroxide as an Efficient Oxygen Evolution Catalyst. *J. Am. Chem. Soc.* **2014**, *136*, 16481−16484.

(17) Liu, Y.; Cheng, H.; Lyu, M.; Fan, S.; Liu, Q.; Zhang, W.; Zhi, Y.; Wang, C.; Xiao, C.; Wei, S.; Ye, B.; Xie, Y. Low Overpotential in Vacancy-Rich Ultrathin $CoSe_2$ Nanosheets for Water Oxidation. *J. Am. Chem. Soc.* **2014**, *136*, 15670−15675.

(18) Zhu, Y.; Zhou, W.; Chen, Z.-G.; Chen, Y.; Su, C.; Tade, M. O.; Shao, Z. $SrNb_{0.1}Co_{0.7}Fe_{0.2}O_{3-\delta}$ Perovskite as a Next-Generation Electrocatalyst for Oxygen Evolution in Alkaline Solution. *Angew. Chem., Int. Ed.* **2015**, *54*, 3897−3901.

(19) Fominykh, K.; Chernev, P.; Zaharieva, I.; Sicklinger, J.; Stefanic, G.; Döblinger, M.; Müller, A.; Pokharel, A.; Böcklein, S.; Scheu, C.; Bein, T.; Fattakhova-Rohlfing, D. Iron-Doped Nickel Oxide Nanocrystals as Highly Efficient Electrocatalysts for Alkaline Water Splitting. *ACS Nano* **2015**, *9*, 5180−5188.

DOI: 10.1021/acsami.6b07209
ACS Appl. Mater. Interfaces 2016, 8, 22534−22544

(20) Liang, Y.; Li, Y.; Wang, H.; Zhou, J.; Wang, J.; Regier, T.; Dai, H. Co_3O_4 Nanocrystals on Graphene as a Synergistic Catalyst for Oxygen Reduction Reaction. *Nat. Mater.* **2011**, *10*, 780−786.
(21) Bajdich, M.; Garcia-Mota, M.; Vojvodic, A.; Norskov, J. K.; Bell, A. T. Theoretical Investigation of the Activity of Cobalt Oxides for the Electrochemical Oxidation of Water. *J. Am. Chem. Soc.* **2013**, *135*, 13521−13530.
(22) Lutterman, D. A.; Surendranath, Y.; Nocera, D. G. A Self-Healing Oxygen-Evolving Catalyst. *J. Am. Chem. Soc.* **2009**, *131*, 3838−3839.
(23) Ahn, H. S.; Tilley, T. D. Electrocatalytic Water Oxidation at Neutral pH by a Nanostructured $Co(PO_3)_2$ Anode. *Adv. Funct. Mater.* **2013**, *23*, 227−233.
(24) Gonzalez-Flores, D.; Sanchez, I.; Zaharieva, I.; Klingan, K.; Heidkamp, J.; Chernev, P.; Menezes, P. W.; Driess, M.; Dau, H.; Montero, M. L. Heterogeneous Water Oxidation: Surface Activity *versus* Amorphization Activation in Cobalt Phosphate Catalysts. *Angew. Chem., Int. Ed.* **2015**, *54*, 2472−2476.
(25) Zhong, D. K.; Gamelin, D. R. Photoelectrochemical Water Oxidation by Cobalt Catalyst (Co-Pi)/r-Fe_2O_3 Composite Photoanodes: Oxygen Evolution and Resolution of a Kinetic Bottleneck. *J. Am. Chem. Soc.* **2010**, *132*, 4202−4207.
(26) Ullman, A. M.; Brodsky, C. N.; Li, N.; Zheng, S. L.; Nocera, D. G. Probing Edge Site Reactivity of Oxidic Cobalt Water Oxidation Catalysts. *J. Am. Chem. Soc.* **2016**, *138*, 4229−4236.
(27) Bao, J.; Zhang, X.; Fan, B.; Zhang, J.; Zhou, M.; Yang, W.; Hu, X.; Wang, H.; Pan, B.; Xie, Y. Ultrathin Spinel-Structured Nanosheets Rich in Oxygen Deficiencies for Enhanced Electrocatalytic Water Oxidation. *Angew. Chem.* **2015**, *127*, 7507−7512.
(28) Liu, Y.; Xiao, C.; Lyu, M.; Lin, Y.; Cai, W.; Huang, P.; Tong, W.; Zou, Y.; Xie, Y. Ultrathin Co_3S_4 Nanosheets that Synergistically Engineer Spin States and Exposed Polyhedra that Promote Water Oxidation under Neutral Conditions. *Angew. Chem., Int. Ed.* **2015**, *54*, 11231−11235.
(29) Gerken, J. B.; McAlpin, J. G.; Chen, J. Y.; Rigsby, M. L.; Casey, W. H.; Britt, R. D.; Stahl, S. S. Electrochemical Water Oxidation with Cobalt-Based Electrocatalysts from pH 0−14: the Thermodynamic Basis for Catalyst Structure, Stability, and Activity. *J. Am. Chem. Soc.* **2011**, *133*, 14431−14442.
(30) Masquelier, C.; Croguennec, L. Polyanionic (phosphates, silicates, sulfates) Frameworks as Electrode Materials for Rechargeable Li (or Na) Batteries. *Chem. Rev.* **2013**, *113*, 6552−6591.
(31) Hu, X. L.; Piccinin, S.; Laio, A.; Fabris, S. Atomic Structure of Cobalt-Phosphate Nanoparticles for Catalytic Water Oxidation. *ACS Nano* **2012**, *6*, 10497−10504.
(32) Liu, Y.; Wang, H.; Lin, D.; Liu, C.; Hsu, P.-C.; Liu, W.; Chen, W.; Cui, Y. Electrochemical Tuning of Olivine-Type Lithium Transition-Metal Phosphates as Efficient Water Oxidation Catalysts. *Energy Environ. Sci.* **2015**, *8*, 1719−1724.
(33) Jin, K.; Park, J.; Lee, J.; Yang, K. D.; Pradhan, G. K.; Sim, U.; Jeong, D.; Jang, H. L.; Park, S.; Kim, D.; Sung, N.-E.; Kim, S. H.; Han, S.; Nam, K. T. Hydrated Manganese(II) Phosphate ($Mn_3(PO_4)_2 \cdot 3H_2O$) as a Water Oxidation Catalyst. *J. Am. Chem. Soc.* **2014**, *136*, 7435−7443.
(34) Kim, H.; Park, I.; Lee, S.; Kim, H.; Park, K.-Y.; Park, Y.-U.; Kim, H.; Kim, J.; Lim, H.-D.; Yoon, W.-S.; Kang, K. Understanding the Electrochemical Mechanism of the New Iron-Based Mixed-Phosphate $Na_4Fe_3(PO_4)_2(P_2O_7)$ in a Na Rechargeable Battery. *Chem. Mater.* **2013**, *25*, 3614−3622.
(35) Kim, H.; Park, J.; Park, I.; Jin, K.; Jerng, S. E.; Kim, S. H.; Nam, K. T.; Kang, K. Coordination Tuning of Cobalt Phosphates towards Efficient Water Oxidation Catalyst. *Nat. Commun.* **2015**, *6*, 8253.
(36) Hoffman, A. E.; De Stefano, M.; Shoen, C.; Gopinath, K.; Warner, D. F.; Cynamon, M.; Doyle, R. P. Co(II) and Cu(II) Pyrophosphate Complexes have Selectivity and Potency against Mycobacteria including Mycobacterium Tuberculosis. *Eur. J. Med. Chem.* **2013**, *70*, 589−593.
(37) Shakoor, R. A.; Kim, H.; Cho, W.; Lim, S. Y.; Song, H.; Lee, J. W.; Kang, J. K.; Kim, Y.-T.; Jung, Y.; Choi, J. W. Site-Specific Transition Metal Occupation in Multicomponent Pyrophosphate for Improved Electrochemical and Thermal Properties in Lithium Battery Cathodes: A Combined Experimental and Theoretical Study. *J. Am. Chem. Soc.* **2012**, *134*, 11740−11748.
(38) Pang, H.; Yan, Z.; Ma, Y.; Li, G.; Chen, J.; Zhang, J.; Du, W.; Li, S. Cobalt Pyrophosphate Nano/Microstructures as Promising Electrode Materials of Supercapacitor. *J. Solid State Electrochem.* **2013**, *17*, 1383−1391.
(39) Forsyth, J. B.; Wilkinson, C.; Paster, S.; Wanklyn, B. M. The Magnetic Structure of Cobalt Diphosphate ($Co_2P_2O_7$). *J. Phys.: Condens. Matter* **1989**, *1*, 169−178.
(40) Zhang, Y.-B.; Wang, D.-Q.; Miao, Z.-Z.; Pan, X.-Q.; Zhang, Z.-D.; Yang, X.-G. Synthesis of *p*-Hydroxybenzaldehyde by Liquid-Phase Catalytic Oxidation of *p*-Cresol over PVDF Modified Cobalt Pyrophosphate. *Chem. Res. Chin. Univ.* **2013**, *29*, 319−323.
(41) Song, S.-Y.; Ma, J.-F.; Yang, J.; Cao, M.-H.; Li, K.-C. Selected-Control Synthesis of Metal Phosphonate Nanoparticles and Nanorods. *Inorg. Chem.* **2005**, *44*, 2140−2142.
(42) Wen, H.; Cao, M.; Sun, G.; Xu, W.; Wang, D.; Zhang, X.; Hu, C. Hierarchical Three-Dimensional Cobalt Phosphate Microarchitectures: Large-Scale Solvothermal Synthesis, Characterization, and Magnetic and Microwave Absorption Properties. *J. Phys. Chem. C* **2008**, *112*, 15948−15955.
(43) Choi, S.-I.; Shao, M.; Lu, N.; Ruditskiy; Peng, H.-C.; Park, J.; Guerrero, S.; Wang, J.; Kim, M. J.; Xia, Y. Synthesis and Characterization of Pd@Pt-Ni Core-Shell Octahedra with High Activity toward Oxygen Reduction. *ACS Nano* **2014**, *8*, 10363−10371.
(44) Jiang, G.; Zhu, H.; Zhang, X.; Shen, B.; Wu, L.; Zhang, S.; Lu, G.; Wu, Z.; Sun, S. Core/Shell Face-Centered Tetragonal FePd/Pd Nanoparticles as an Efficient Non-Pt Catalyst for the Oxygen Reduction Reaction. *ACS Nano* **2015**, *9*, 11014−11022.
(45) Hunt, S. T.; Milina, M.; Alba-Rubio, A. C.; Hendon, C. H.; Dumesic, J. A.; Román-Leshkov, Y. Self-assembly of Noble Metal Monolayers on Transition Metal Carbide Nanoparticle Catalysts. *Science* **2016**, *352*, 974−978.
(46) Wang, J.; Wu, H.; Gao, D.; Miao, S.; Wang, G.; Bao, X. High-Density Iron Nanoparticles Encapsulated within Nitrogen-Doped Carbon Nanoshell as Efficient Oxygen Electrocatalyst for Zinc-Air Battery. *Nano Energy* **2015**, *13*, 387−396.
(47) Cui, X.; Ren, P.; Deng, D.; Deng, J.; Bao, X. Single Layer Graphene Encapsulating Non-precious Metals as High-Performance Electrocatalysts for Water Oxidation. *Energy Environ. Sci.* **2016**, *9*, 123−129.
(48) Yang, W.; Liu, X.; Yue, X.; Jia, J.; Guo, S. Bamboo-like Carbon Nanotube/Fe_3C Nanoparticle Hybrids and Their Highly Efficient Catalysis for Oxygen Reduction. *J. Am. Chem. Soc.* **2015**, *137*, 1436−1439.
(49) Zhang, Y.; Jiang, W.-J.; Guo, L.; Zhang, X.; Hu, J.-S.; Wei, Z.; Wan, L.-J. Confining Iron Carbide Nanocrystals inside CNx@CNT toward an Efficient Electrocatalyst for Oxygen Reduction Reaction. *ACS Appl. Mater. Interfaces* **2015**, *7*, 11508−11515.
(50) Zheng, Y. R.; Gao, M. R.; Gao, Q.; Li, H. H.; Xu, J.; Wu, Z. Y.; Yu, S. H. An Efficient $CeO_2/CoSe_2$ Nanobelt Composite for Electrochemical Water Oxidation. *Small* **2015**, *11*, 182−188.
(51) Deng, J.; Ren, P.; Deng, D.; Bao, X. Enhanced Electron Penetration through an Ultrathin Graphene Layer for Highly Efficient Catalysis of the Hydrogen Evolution Reaction. *Angew. Chem., Int. Ed.* **2015**, *54*, 2100−2104.
(52) Shen, M.; Ruan, C.; Chen, Y.; Jiang, C.; Ai, K.; Lu, L. Covalent Entrapment of Cobalt-Iron Sulfides in N-Doped Mesoporous Carbon: Extraordinary Bifunctional Electrocatalysts for Oxygen Reduction and Evolution Reactions. *ACS Appl. Mater. Interfaces* **2015**, *7*, 1207−1218.
(53) Indra, A.; Menezes, P. W.; Sahraie, N. R.; Bergmann, A.; Das, C.; Tallarida, M.; Schmeisser, D.; Strasser, P.; Driess, M. Unification of Catalytic Water Oxidation and Oxygen Reduction Reactions: Amorphous Beat Crystalline Cobalt Iron Oxides. *J. Am. Chem. Soc.* **2014**, *136*, 17530−17536.

DOI: 10.1021/acsami.6b07209
ACS Appl. Mater. Interfaces 2016, 8, 22534−22544

(54) Gorlin, Y.; Jaramillo, T. F. A Bifunctional Nonprecious Metal Catalyst for Oxygen Reduction and Water Oxidation. *J. Am. Chem. Soc.* **2010**, *132*, 13612−13614.
(55) McCrory, C. C.; Jung, S.; Peters, J. C.; Jaramillo, T. F. Benchmarking Heterogeneous Electrocatalysts for the Oxygen Evolution Reaction. *J. Am. Chem. Soc.* **2013**, *135*, 16977−16987.
(56) Tüysüz, H.; Hwang, Y. J.; Khan, S. B.; Asiri, A. M.; Yang, P. Mesoporous Co_3O_4 as an Electrocatalyst for Water Oxidation. *Nano Res.* **2013**, *6*, 47−54.
(57) Cheng, N.; Liu, Q.; Tian, J.; Xue, Y.; Asiri, A. M.; Jiang, H.; He, Y.; Sun, X. Acidically Oxidized Carbon Cloth: a Novel Metal-Free Oxygen Evolution Electrode with High Catalytic Activity. *Chem. Commun.* **2015**, *51*, 1616−1619.
(58) Zhao, Z.; Wu, H.; He, H.; Xu, X.; Jin, Y. A High-Performance Binary Ni-Co Hydroxide-based Water Oxidation Electrode with Three-Dimensional Coaxial Nanotube Array Structure. *Adv. Funct. Mater.* **2014**, *24*, 4698−4705.
(59) Wang, H.; Li, Z.; Li, G.; Peng, F.; Yu, H. Co_3S_4/NCNTs: A Catalyst for Oxygen Evolution Reaction. *Catal. Today* **2015**, *245*, 74−78.
(60) Zhuang, Z.; Sheng, W.; Yan, Y. Synthesis of Monodispere Au@Co_3O_4 Core-Shell Nanocrystals and Their Enhanced Catalytic Activity for Oxygen Evolution Reaction. *Adv. Mater.* **2014**, *26*, 3950−3955.
(61) Zheng, Y. L.; Zhao, S. L.; Liu, S. L.; Yin, H. H.; Chen, Y.-Y.; Bao, J. C.; Han, M.; Dai, Z. H. Component-Controlled Synthesis and Assembly of Cu-Pd Nanocrystals on Graphene for Oxygen Reduction Reaction. *ACS Appl. Mater. Interfaces* **2015**, *7*, 5347−5357.
(62) Hunault, M.; Robert, J.-L.; Newville, M.; Galoisy, L.; Calas, G. Spectroscopic Properties of Five-Coordinated Co^{2+} in Phosphates. *Spectrochim. Acta, Part A* **2014**, *117*, 406−412.
(63) Meseguer, S.; Tena, M. A.; Gargori, C.; Badenes, J. A.; Llusar, M.; Monros, G. Structure and Colour of Cobalt Ceramic Pigments from Phosphates. *Ceram. Int.* **2007**, *33*, 843−849.

DOI: 10.1021/acsami.6b07209
ACS Appl. Mater. Interfaces 2016, 8, 22534−22544